Results of downhole microseismic monitoring at a pilot hydraulic fracturing site in Poland — Part 2: S-wave splitting analysis

Wojciech Gajek[1], Michał Malinowski[1], and James P. Verdon[2]

Abstract

Observations of azimuthal seismic anisotropy provide useful information, notably on stress orientation and the presence of preexisting natural fracture systems, during hydraulic fracturing operations. Seismic anisotropy can be observed through the measurement of S-wave splitting (SWS) on waveforms generated by microseismic events and recorded on downhole geophone arrays. We have developed measurements of azimuthal anisotropy from a Lower Paleozoic shale play in northern Poland. The observed orthorhombic anisotropic symmetry system is dominated by a vertically transverse isotropy (VTI) fabric, produced by the alignment of anisotropic platy clay minerals and by thin horizontal layering and overprinted by a weak azimuthal anisotropy. Despite the dominating VTI fabric, we successfully identified a weaker horizontal-transverse isotropy fabric striking east–southeast. We do this by constraining the rock-physics model inversion with VTI background parameters incorporated from other geophysical methods: microseismic velocity model inversion, 3D reflection seismic, and borehole cross-dipole sonic logs. The obtained orientation is consistent with a preexisting natural fracture set that has been observed using X-ray micro-imaging (XRMI) image logs from a nearby vertical well. The present-day regional maximum horizontal stress direction differs from the observed fracture strike by approximately 45°. This implies that the SWS measurements recorded during hydraulic stimulation of a shale-gas reservoir are imaging the preexisting natural fracture set, which influences the treatment efficiency, instead of the present-day stress.

Introduction

Most rocks display some degree of seismic anisotropy. There are numerous well-known mechanisms causing anisotropy at various scales, including preferred mineral or crystal orientation (Johnston and Christensen, 1995; Lonardelli et al., 2007; Hall et al., 2008), sedimentary layering (Backus, 1962; Liu and Martinez, 2012), aligned fracture sets (Hudson, 1981; Naar et al., 2006), and the application of anisotropic stresses (Lynn and Thomsen, 1986; Verdon et al., 2008). One of the most direct indicators of anisotropy is an S-wave splitting (SWS), in which an S-wave propagating through anisotropic medium is split into two orthogonally polarized S-waves traveling with different velocities (Ando et al., 1980; Crampin et al., 1980). The polarity of the fast and slow arrivals and the delay times between the two S-waves will be determined by the anisotropic symmetry system and the direction of wave propagation relative to this symmetry system. The delay time will also be determined by the strength of the anisotropy (e.g., Verdon et al., 2009).

SWS has been exploited in various settings to retrieve important features of the subsurface at various scales. It is observed in laboratory tests on stressed or fractured rocks (Nur and Simmons, 1969; Xu and King, 1989; Ebrom et al., 1990, Tillotson et al., 2012), as well as in global seismology for long-period waves propagating through the crust and mantle (e.g., Vinnik et al., 1989; Silver and Chan, 1991; Savage, 1999). After being recognized as a useful phenomenon at the exploration scale (Crampin, 1985; Lynn and Thomsen, 1986; Willis et al., 1986), SWS has been used in fracture detection from surface seismic (Martin and Davis, 1987; Mueller, 1991; Liu and Martinez, 2012) and multicomponent and walkaway vertical seismic profiling (VSP) (Lynn et al., 1999; MacBeth, 2002; Horne, 2003). SWS is also conventionally used in cross-dipole sonic logging for measuring in situ azimuthal S-wave anisotropy around the borehole (Mueller et al., 1994; Patterson and Tang, 2001).

Two split shear modes are frequently observed during 3C downhole microseismic monitoring in hydrocarbon reservoirs. This length scale is usefully positioned between the laboratory scale and larger scale seismic observations (Verdon and Wuestefeld, 2013). Unlike VSP and reflection seismic imaging, measuring SWS with downhole receivers benefits from the proximity of seismic sources (microearthquakes) and receiver

[1]Institute of Geophysics Polish Academy of Sciences, Warsaw, Poland. E-mail: wgajek@igf.edu.pl; michalm@igf.edu.pl.
[2]University of Bristol, School of Earth Sciences, Bristol, UK. E-mail: james.verdon@bristol.ac.uk.

Manuscript received by the Editor 23 November 2017; revised manuscript received 28 May 2018; published ahead of production 08 June 2018; published online 23 July 2018. This paper appears in *Interpretation*, Vol. 6, No. 3 (August 2018); p. SH49–SH58, 9 FIGS., 1 TABLE.
http://dx.doi.org/10.1190/INT-2017-0207.1.

arrays. Hence, it can be efficiently used to image anisotropy within the reservoir without the overburden influence that affects other methods (Wuestefeld et al., 2011).

Measurements of seismic anisotropy from microseismicity can be used in several ways, including improving the accuracy of the velocity model (e.g., Grechka et al., 2011), enhancing the precision of event locations (Grechka and Yaskevich, 2014), investigation of fracture alignment (e.g., Miyazawa et al., 2008; Verdon and Kendall, 2011) and fracture connectivity (e.g., Baird et al., 2013; Verdon and Wuestefeld, 2013), and determining changing stress conditions generated by subsurface operations (e.g., Verdon et al., 2011). Measurements of seismic anisotropy have been used in the geothermal industry (e.g., Rial et al., 2005) and for carbon capture and storage (e.g., Verdon et al., 2011), although its most common application with respect to microseismic data is during hydraulic fracturing of shale and tight gas reservoirs (e.g., Verdon and Wuestefeld, 2013).

The dominant symmetry system for many shales is a vertical-transverse isotropy (VTI) fabric. In a VTI system, wave velocities are independent of azimuth and depend solely on the angle of ray propagation from vertical. VTI fabrics can be described by the Thomsen (1986) parameters ε, γ, and δ under the weak-anisotropy condition. In shales, this VTI system is generated by the alignment of platy, anisotropic clay minerals within the sedimentary layers (e.g., Kendall et al., 2007). Horizontal-transverse isotropy (HTI) describes a medium when velocity depends on the azimuth of propagation. HTI can be created by the presence of aligned vertical fracture sets (Gupta, 1973; Crampin, 1985). Sedimentary rocks usually contain a combination of VTI and HTI fabrics, creating orthorhombic symmetry (Tsvankin, 1997; Grechka, 2007). In shales and mudstones, the VTI fabric can be particularly strong, obscuring the weaker effects of azimuthal anisotropy (e.g., Baird et al., 2018). As such, identifying the effects of sedimentary fabrics to reveal the presence of fractures can be challenging.

In this paper, we present a case study from the northern Poland Lower Paleozoic shale play, where hydraulic stimulation was monitored using a downhole geophone array. We perform SWS analysis to image the azimuthal anisotropy in the reservoir. The VTI fabric dominates over the weaker azimuthal anisotropy and hinders the constraint of vertical fracture parameters during an inversion of orthorhombic anisotropic model. However, by incorporating the VTI fabric constrained by (1) 3D reflection seismic surveying, (2) sonic log analysis, and (3) microseismic event location analysis into our inversion procedure, we are able to obtain constrained measurements of the azimuthal seismic anisotropy within the orthorhombic symmetry system.

The first part of the paper (Gajek et al., 2018) introduces the experiment setting, geology, and monitoring array geometry. It presents a VTI velocity model inversion based on recorded perforation shots, location of microseismic events, and hydraulic fracturing job effectiveness assessment.

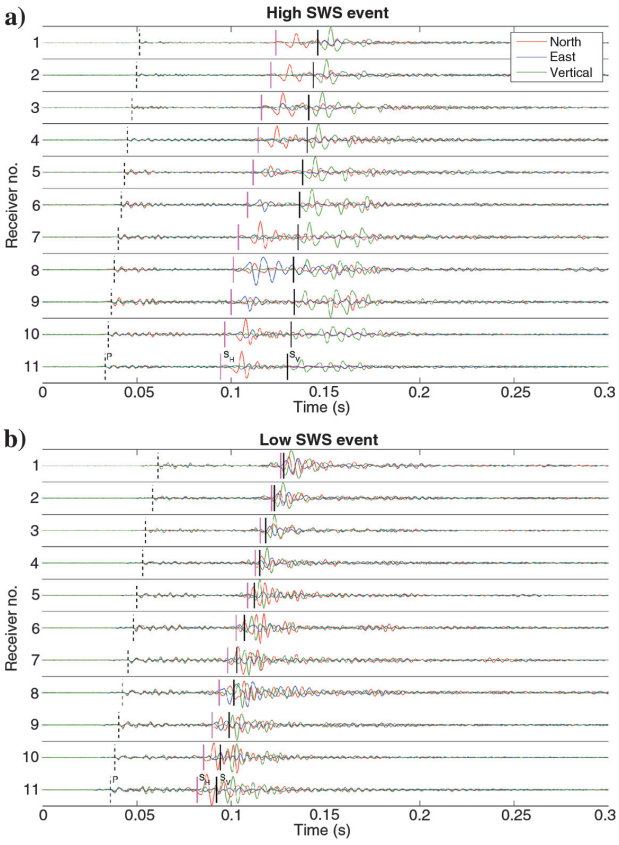

Figure 1. Waveforms from example microseismic events recorded by the 11 3C geophones. (a) An event with strong SWS, producing significant time delays (19–37 ms) between fast and slow S-waves. The event is located 450 m from the monitoring array. (b) An event with smaller amounts of SWS. The event is located 305 m from the monitoring array. Picks are labeled on bottom traces.

Data and methods

In our case study, six stages of hydraulic fracturing were monitored using an 11-receiver downhole geophone array located in a vertical observation well near the heel of the horizontal injection well. Example waveforms with strong and weak SWS are shown in Figure 1. Most of the recorded events had clear strong SH-wave arrivals and weaker P-wave arrivals. SWS was visible on most of the records — at least one-third of the events had clear SV-wave onsets. A detailed description of the site, geometry, data processing, and VTI model inversion can be found in Gajek et al. (2018). The anisotropy is manifested by a significant, stage-varying SWS (up to 40 ms for some of the events), necessitating the use of an anisotropic velocity model for the purpose of microseismic event location. A 1D five-layer VTI model was built using traveltimes from 13 perforation shots and selected microseismic events. The model consisted of layer-dependent velocities and effective Thomsen's parameters for all layers. Finally, detected events were

located by inverting picked traveltimes, using a Bayesian approach (e.g., Tarantola, 2005; Gajek et al., 2016).

SWS measurements provide the polarization Φ of the fast S-wave, and the time delay dt between the two split shear modes (Wolfe and Silver, 1998; Teanby et al., 2004). A measurement can be made for each source-receiver pair, resulting in considerable amount of data when the geophone array is used to record hundreds of events. To deal with the large number of measurements thus required, we use the automated method described by Wuestefeld et al. (2010), which is based in turn on that described by Teanby et al. (2004). The workflow is presented in Figure 2. Recorded waveforms are rotated to the ray-frame coordinates to minimize P-wave energy on the qSH and qSV components. Next, the SWS correction is applied, resulting in a linearization of the particle motion in a fast- and slow-axis coordinate system (Figure 2c). The SWS correction is determined by applying all possible fast S-wave orientations and time shifts and then retrieving the minimum error solution from the resulting error surface (Figure 2d). The analysis is performed for various-length S-wave windows to provide a stable solution regardless of window position and length (Figure 2e). A more detailed description of this workflow is described in the Figure 2 caption.

To ensure good data quality, the acceptance criteria defined by Teanby et al. (2004) were used to ensure that only robust SWS measurements were taken forward for further analysis, including

- good event signal-to-noise ratio (S/N)
- linear P-wave motion allowing a well-constrained rotation from a geographical (N-E-Z) to a ray-frame (qP-qSH-qSV) coordinate system
- effective minimization of energy on the transverse component after the SWS correction has been applied, resulting in linear postcorrection particle motion and matching postcorrection waveforms in a fast- and slow-S-wave coordinate system
- a single, tightly constrained minimum in the error surface
- consistent SWS results regardless of the choice of the analysis window start time and length.

A good-quality result must fulfil all of these conditions. These criteria were first assessed automatically

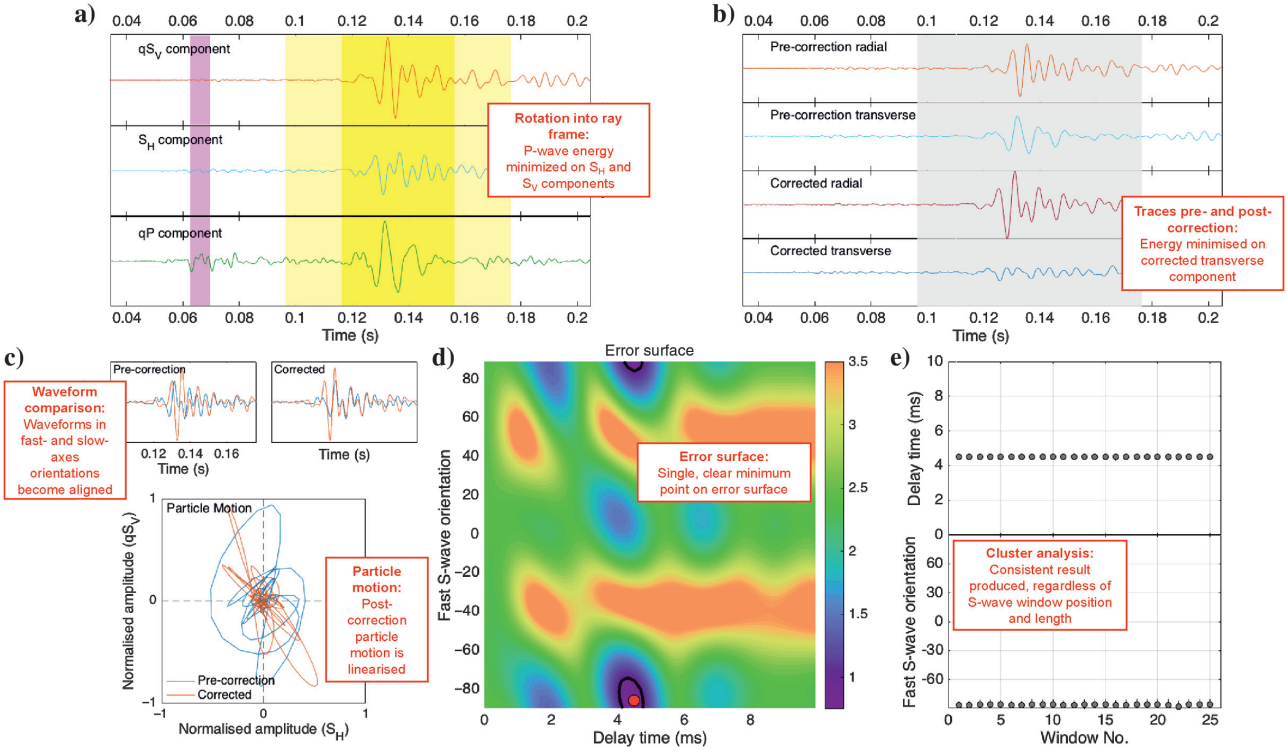

Figure 2. Example SWS result, showing the QC criteria used to assess the measurements. In (a), we plot the recorded waveforms in the ray-frame coordinates: An effective rotation will ensure that P-wave energy is minimized on the qSH and qSV components. In (b), we plot the radial and transverse components prior to and after the SWS correction have been applied: the SWS correction should minimize energy on the transverse component. In (c), we plot the S-wave arrivals in the SWS fast- and slow-orientation coordinates, and the pre and postcorrection particle motion (a superposition of components plotted in [b] restricted to the longest analysis window length): After correction, two matching waveforms should be found, resulting in a linearization of the particle motion. In (d), we plot the error surface of the correction method as a function of delay time and fast direction, normalized such that the 95% confidence (highlighted in bold) interval is one: A single, clear minimum point should be produced. In (e), we compare SWS results produced by altering the analysis windows within the light- and dark-yellow bands of (a). A good result should be consistent regardless of the choice of analysis window.

by discarding results, which evidently neglected any of these conditions. Then, remaining SWS measurements were assessed manually via the inspection of figures, such as that shown in Figure 2.

Inversion of SWS measurements for rock-physics parameters

A single measurement of dt and Φ along a single raypath is not sufficient to constrain the overall anisotropic symmetry system. Instead, a population of SWS measurements along a range of raypaths must be inverted to reveal the overall anisotropy. Typically, a rock-physics model, assuming a particular anisotropic symmetry system, must be created, which is then compared with the observations, with the best-fitting rock-physics model parameterization being taken as the result (e.g., Verdon et al., 2009).

In this case, we inverted measured fast polarization angles and time delays for a background VTI fabric (Thomsen, 2002) overprinted with a single set of vertically aligned, unfilled, penny-shaped fractures (Hudson, 1981), resulting in effective orthorhombic symmetry. The inversion is resolved for four free parameters of the effective orthorhombic medium between receivers and microseismic sources:

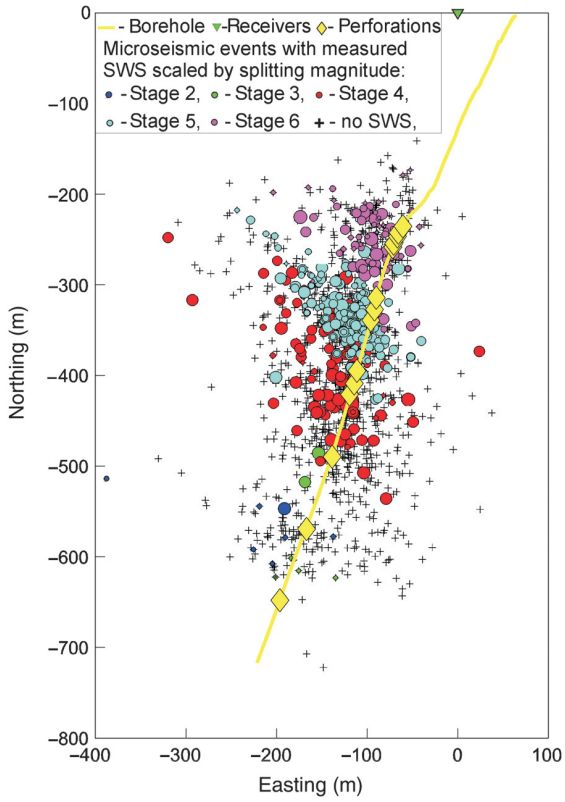

Figure 3. A map view of stage-colored microseismic events locations with at least one good-quality SWS measurement, scaled by the splitting magnitude. Other microseismic events are marked as black plus signs at the background.

- The fracture density ξ and strike α of the vertical fracture set.
- Thomsen's parameters describing the VTI rock fabric.
- With only S-wave data, δ and ε cannot be constrained independently; Instead, a ratio between δ and ε is resolved.

The inversion is performed following the method described by Verdon et al. (2009) and Verdon and Wuestefeld (2013). When iterating over a parameter space (ξ, α, δ, and γ), the elastic stiffness tensor providing velocities and polarizations of S-waves for any direction is computed by solving a Christoffel equation, independent from Thomsen's (1986) weak anisotropy assumption. The background P- and S-wave velocities, V_{P0}, V_{S0}, and density are held constant through the model space. Velocities are based on the VTI velocity model described by Gajek et al. (2018), whereas the mean density was taken from the well-log interval of interest.

Results

Out of more than 14,000 SWS measurements, 561 were accepted as good-quality results under our strict acceptance criteria. The spatial distribution of microseismic events with a good-quality measurement on at least one trace is plotted in Figure 3 in map view and in Figure 4 in side view. Significant noise levels restricted the number of good measurements, especially for distant stages: Only 4% of accepted measurements belonged to stages 1–3 (the most distant from the observation well). The accepted measurements had approximately 35° wide azimuthal coverage and 35°–70° incidence angle coverage (Figure 5a and 5b). Most fast S-wave polarization angles are at 90° relative to the qSV orientation; i.e., they are near-horizontal, as expected from a VTI system. However, significant numbers of events do not have horizontal fast S-wave polarizations, and indeed the delay times for these events are often larger than the delay times for those with horizontal polarizations (Figure 5c). These observations imply that the system is not solely VTI. Instead, such a signature can be recognized as VTI fabric influenced by vertical fractures (Usher et al., 2015).

The inversion of SWS measurements for an orthorhombic rock-physics model without any prior VTI fabric constraints resulted in unstable fracture parameters (strike α and crack density ξ). Those parameters were not constrained because the relatively weaker azimuthal anisotropy did not contribute significantly to the overall model due to limited azimuthal and incidence angle data coverage (Verdon et al., 2009) and stronger VTI fabric that dominates the inversion (Gajek et al., 2017).

However, the VTI fabric has already been observed by other geophysical methods, including (1) 3D VTI prestack depth migration velocity model (Kowalski et al., 2014) from a coincident 3D seismic survey, for which γ was derived using n empirical relation to ε (Wang,

2001), (2) Backus-averaged well logs, and (3) the velocity model inverted for microseismic event location, described by Gajek et al. (2018). Sonic, density, and natural gamma logs were used to obtain the vertical velocities V_{P0} and V_{S0}, and to derive Thomsen's (1986) parameters. Those parameters were downscaled to 200 Hz using a Backus (1962) averaging scheme. The VTI parameters for three models are listed in Table 1. There is some disagreement between the prior VTI measurements. Therefore, we explored the effect on the fracture parameters (α and ξ) inverted from SWS measurements when the VTI fabric is fixed, doing this using each of the VTI fabrics determined from each of the geophysical methods (reflection seismic, well log, and microseismic). The results are listed in Table 1.

We find that, within the range of possible VTI parameters defined by the seismic, well log, and microseismic observations, and then, inversion for fracture strikes and densities are well-constrained and consistent, ranging between 102°–108° and 0.09°–0.14°, respectively (Figure 6).

Discussion

We assumed a VTI medium influenced by vertical cracks after judging from S-wave delay times and the corresponding incidence angle (Figure 5c). However, for particular solely VTI settings, the SV-wave can propagate faster than the SH-wave toward particular directions (Thomsen, 1986). Nevertheless, we excluded this possibility basing on a synthetic model of SH- and SV-wave velocities in a VTI medium (Figure 7). Two scenarios for the strongest ($\gamma = 0.27$) and the weakest ($\gamma = 0.14$) anisotropy among the finally obtained models (Table 1) were tested, with common parameters: $V_{S0} = 2400$ m/s, $\varepsilon = 0.15$, $\delta = 0.02$. For these particular VTI media, the SV-wave can be slightly faster than the SH-wave in the case of the lower anisotropy scenario. However, in the range of incidence angles sampled by SWS measurements, the SH-wave velocity prevails; hence, the assumption of VTI fabric with vertical cracks remains valid.

The observation well is close to the heel of the injection well, whereas the fracturing stages proceeded from the toe to the heel, as is common practice during hydraulic fracturing operations. Such geometry promotes the influence of final stages of the stimulation by limiting the amount of events from

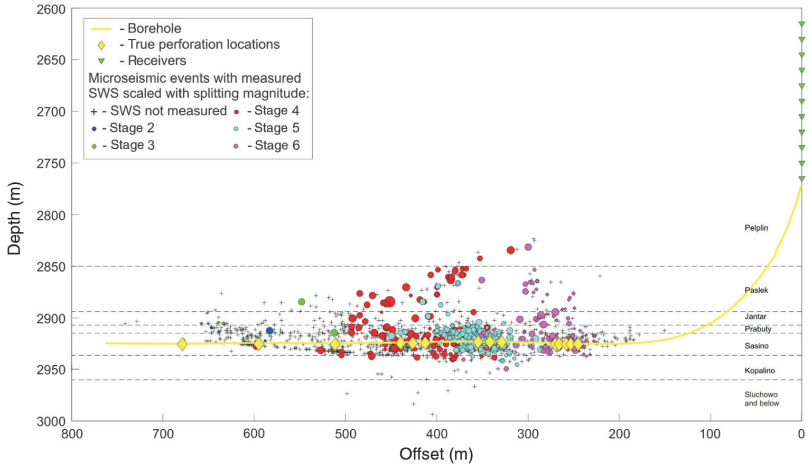

Figure 4. Locations of stage-colored microseismic events with at least one good-quality SWS measurement, scaled by the splitting magnitude. Other microseismic events are marked as black plus signs at the background. Cross section along the borehole trajectory. Primary and secondary target intervals with enhanced TOC concentration are Sasino and Jantar, respectively.

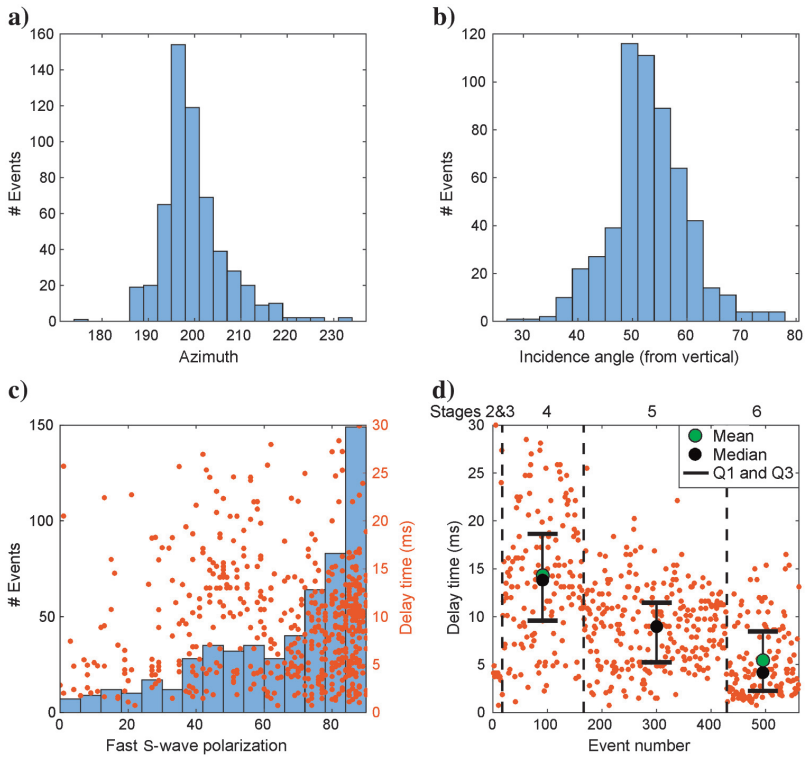

Figure 5. The SWS results for the good-quality measurements. (a) A histogram of P-wave back azimuths, (b) a histogram of raypath incidence angles, and (c) a histogram of the absolute value of the fast direction angles (relative to the qSV orientation). Corresponding delay times are plotted on the secondary axis with orange dots and (d) dt ordered by event origin time (orange dots) and its statistics per stage. Consecutive stages are separated by the dashed line. Note the median and mean for stage 5 overlap. The population of measurements from stages 2 and 3 is insufficient to provide reliable statistics.

Table 1. Comparison of the input VTI parameters as derived from three geophysical methods and the resulting best-fit values for fracture strike and fracture density.

	Input model	Surface seismic	Backus-averaged well log	Microseismic
Input	Epsilon ε	0.17	0.14	0.15
	Gamma γ	0.15	0.14	0.27
	Delta δ	0.11	0.02	0.02
Results	Fracture strike	102°	108°	102°
	Fracture density	0.09	0.14	0.10

initial stages due to the S/N decay with the distance (Figure 4). What is more, it limits the available azimuthal coverage of splitting measurements, in which maximum azimuthal span is provided mostly by events within the closest, i.e., final, stages (Figure 3). Consequently, the unconstrained inversion of the rock-physics parameters did not produce a stable result.

The inversion became well-resolved after fixing the model's VTI parameters. The geophysical data sources used to constrain the inversion vary significantly

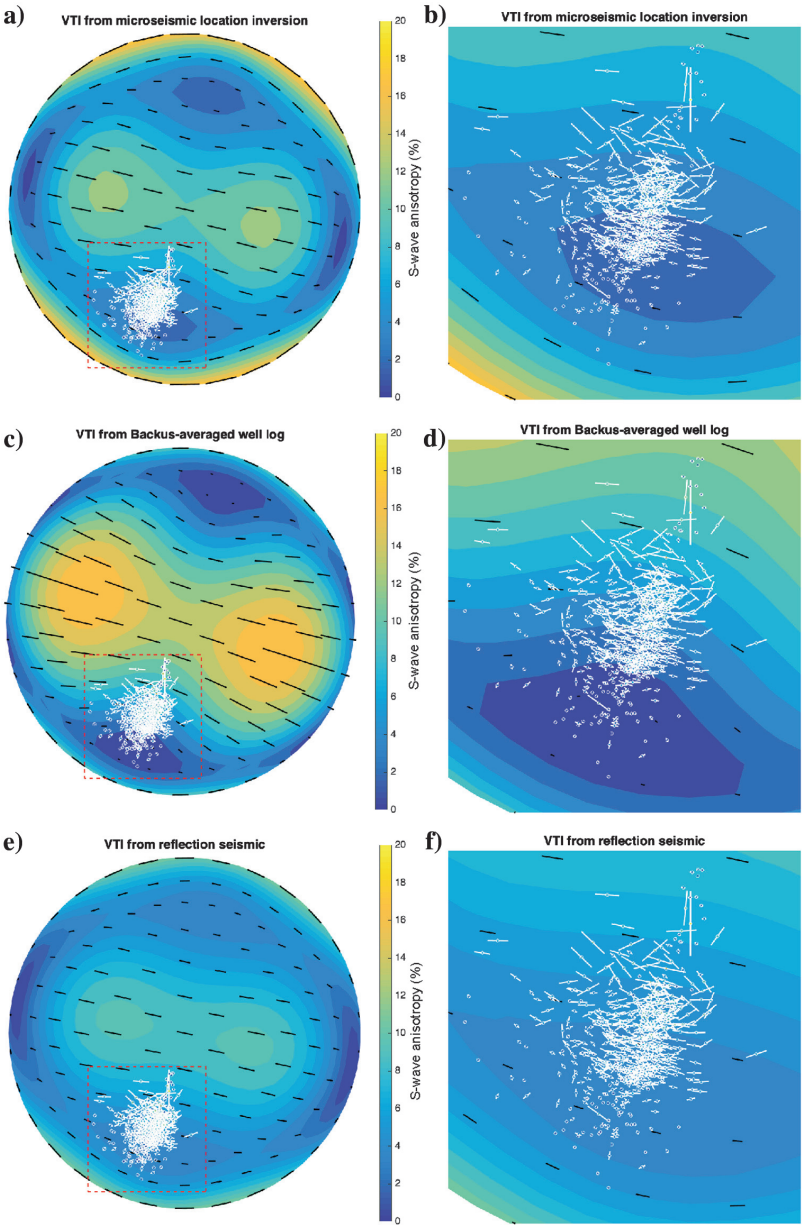

Figure 6. Upper hemisphere projections of measured SWS data (white ticks) and the best fitting rock-physics models (black ticks and background contours). The tick position indicates the azimuth and inclination of the ray-path, the tick orientation indicates the fast S-wave polarization, and colors and tick mark lengths indicate the magnitude of anisotropy. In (a), we show the result using the background VTI parameters derived from reflection seismic data, whereas (b) shows the same data magnified into the red box marked in (a), allowing the data to be inspected in more detail. In (c and d), we show the same for the case with background VTI parameters derived from the Backus-averaged well log, and in (e and f), we show the same for the case with background VTI parameters derived from the microseismic location velocity model.

in scale from seismic frequencies, through microseismic frequencies and up to sonic logs (downscaled to 200 Hz by Backus [1962] averaging). Nevertheless, the obtained fractures strike and fracture density were constrained well for all three models (Figure 8).

The fracture strike of 102°–108° obtained using SWS data is close to the approximately 125° strike of the J2 fracture set obtained from XRMI log interpretation presented in Figure 9 (Bobek and Jarosiński, 2018). The J2 set has biggest contribution to the interval influencing SWS measurements and dominates in the Sasino Formation (see Figure 7b in Gajek et al., 2018). It also contributes to the azimuthal anisotropy as detected by 3D wide-azimuth P-wave seismic data, where similar fracture strikes were inferred (Cyz and Malinowski, 2018). The estimated fracture strike can be influenced by a secondary fracture set J' striking approximately 80°; however, trying to invert for two fracture sets did not result in any stable strike of the second fracture set.

The imaged direction differs by 45°–50° from the in situ regional maximum horizontal stress orientation, which has an azimuth approximately 155° (Jarosiński, 2005). This indicates that the SWS measurements are imaging preexisting natural fractures rather than new fractures created during stimulation, which would be expected to strike parallel to the maximum horizontal stress. However, this is to be expected when the geometry of observation and injection wells is considered: The raypaths from each of the stages are predominantly through the unstimulated rock ahead (i.e., "heel-wards") of the stimulation stages and, therefore, can only image the preexisting natural fractures.

Baird et al. (2013) show how the anisotropic system can change as hydraulic fracturing proceeds and raypaths switch from propagation through unstimulated rock to rocks that have been stimulated, resulting in a change in the dominant fracture strike from that of the preexisting fractures to that of the present-day maximum horizontal stress direction (and the presumed orientation of the hydraulic fractures). Baird et al. (2013) also note an increase in the fracture compliance ratio (Z_N/Z_T) representing the change from partially filled and poorly connected old fractures to the "clean," well-connected new hydraulic fractures. To replicate such measurements, raypaths through the already-stimulated volumes are required, which in turn would require an observation well at the toe end of the injection well for this particular well configuration.

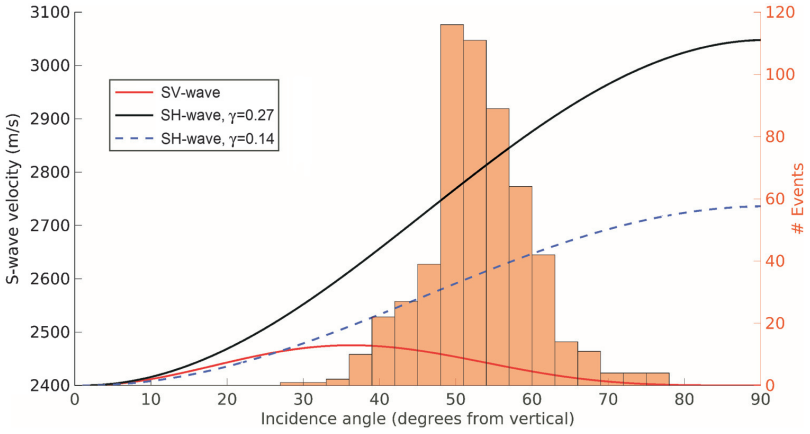

Figure 7. Velocity (independent from γ) marked in the red solid line; SH-wave velocity for the higher anisotropy scenario ($\gamma = 0.27$) marked in the solid black line; SH-wave velocity for the lower anisotropy scenario ($\gamma = 0.14$) marked in the dashed blue line. At the background, a histogram of raypath incidence angles of registered microseismic events is presented (right ordinate) indicating the range of incidence angles sampled by SWS measurements.

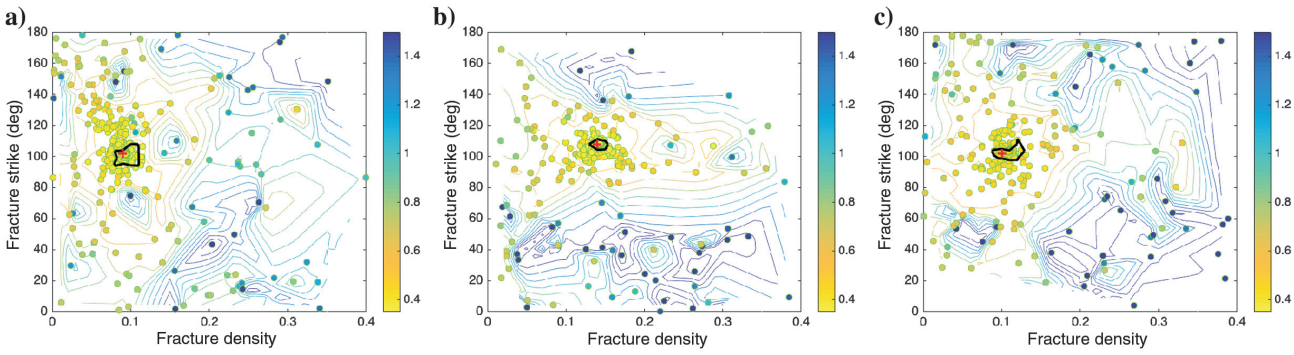

Figure 8. Normalized misfit between the observed SWS and model values as a function of fracture density and strike, with background VTI parameters determined by (a) reflection seismic data, (b) Backus-averaged well log, and (c) the microseismic event location velocity model. The best-fit model in each case is marked by the red +, the green-edged dots mark the model parameters sampled by the neighborhood algorithm while searching for the best-fit model, and the contours represent smoothed misfit surfaces fitted to these sample points, with the solid black line delineating the 95% confidence interval.

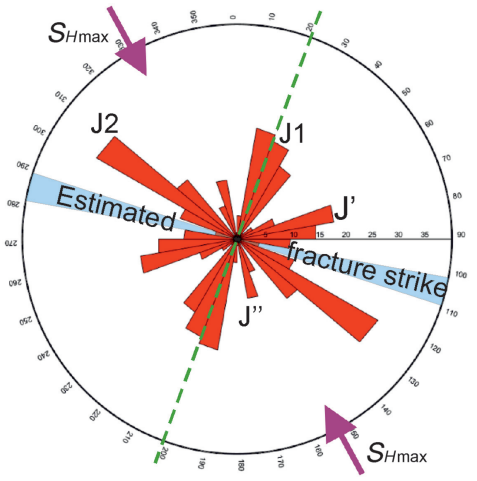

Figure 9. Orientation of the subvertical fracture sets (joints) in the monitoring borehole obtained from XRMI log interpretation (the interval contributing to SWS measurements), the present-day maximum horizontal stress direction ($S_{H\,\max}$), and the estimated fracture strike. The dashed green line points to the direction of the stimulated borehole horizontal segment.

Conclusion

We have performed SWS analysis to invert for fracture parameters during the pilot hydraulic stimulation of the Lower Paleozoic shale target located in Northern Poland. The stimulated shale displays orthorhombic anisotropy with dominant VTI fabric overprinted by weaker azimuthal anisotropy. The imprint of the VTI fabric makes the inversion for fracture parameters harder than it otherwise would be. However, by incorporating constraints on VTI parameters from other geophysical measurements, we are able to invert the observed SWS measurements for a well-constrained estimate of fracture strike of 102°–108° and fracture density of 0.09–0.14. The resulting fracture strike corresponds to the orientation of preexisting fractures obtained from the XRMI log and from the analysis of the surface seismic data, but it is different from the fracture orientation expected from hydraulic fracturing based on the regional maximum horizontal stress direction.

Acknowledgments

This research was conducted within the ShaleMech project funded by the Polish National Centre for Research and Development (NCBR), grant no. BG2/SHALEMECH/14. Data were provided by the PGNiG SA. Collaboration with University of Bristol was supported within TIDES COST Action ES1401. XRMI and cross-dipole sonic interpretation was performed by the Institute of Oil and Gas–National Research Institute. We thank the associate editor, A. Pasternacki, as well as the anonymous reviewers for their useful comments.

References

Ando, M., Y. Ishikawa, and H. Wada, 1980, S-wave anisotropy in the upper mantle under a volcanic area in Japan: Nature, **286**, 43–46, doi: 10.1038/286043a0.

Backus, G. E., 1962, Long-wave elastic anisotropy produced by horizontal layering: Journal of Geophysical Research, **67**, 4427–4440, doi: 10.1029/JZ067i011p04427.

Baird, A. F., J.-M. Kendall, Q. J. Fisher, and J. Budge, 2018, The role of texture, cracks, and fractures in highly anisotropic shales: Journal of Geophysical Research: Solid Earth, **122**, 10341–10351, doi: 10.1002/2017JB014710.

Baird, A. F., J.-M. Kendall, J. P. Verdon, A. Wuestefeld, T. E. Noble, Y. Li, M. Dutko, and Q. J. Fisher, 2013, Monitoring increases in fracture connectivity during hydraulic stimulations from temporal variations in shear wave splitting polarization: Geophysical Journal International, **195**, 1120–1131, doi: 10.1093/gji/ggt274.

Bobek, K., and M. Jarosiński, 2018, Parallel structural interpretation of drill cores and microresistivity scanner images from gas-bearing shale (Baltic Basin, Poland): Interpretation, **6**, no. 3, doi: 10.1190/int-2017-0211.1.

Crampin, S., 1985, Evaluation of anisotropy by shear-wave splitting: Geophysics, **50**, 142–152, doi: 10.1190/1.1441824.

Crampin, S., R. Evans, B. Üçer, M. Doyle, J. P. Davis, G. B. Yegorkina, and A. Miller, 1980, Observations of dilatancy-induced polarization anomalies and earthquake prediction: Nature, **286**, 874–877, doi: 10.1038/286874a0.

Cyz, M., and M. Malinowski, 2018, Seismic azimuthal anisotropy study of the Lower Paleozoic shale play in Northern Poland: Interpretation, **6**, no. 3, doi: 10.1190/int-2017-0200.1.

Ebrom, D., R. Tatham, K. K. Sekharan, J. A. McDonald, and G. H. F. Gardner, 1990, Hyperbolic traveltime analysis of first arrivals in an azimuthally anisotropic medium: A physical modeling study: Geophysics, **55**, 185–191, doi: 10.1190/1.1442825.

Gajek, W., M. Malinowski, and J. P. Verdon, 2018, Results of the downhole microseismic monitoring at a pilot hydraulic fracturing site in Poland — Part 1: Events location and stimulation performance: Interpretation, **6**, no. 3, doi: 10.1190/int-2017-0205.1.

Gajek, W., J. Trojanowski, and M. Malinowski, 2016, Advantages of probabilistic approach to microseismic events location — A case study from Northern Poland: 78th Annual International Conference and Exhibition, EAGE, Extended Abstracts, doi: 10.3997/2214-4609.201600909.

Gajek, W., J. P. Verdon, M. Malinowski, and J. Trojanowski, 2017, Imaging seismic anisotropy in a shale gas reservoir by combining microseismic and 3D surface reflection seismic data: 79th Annual International Conference and Exhibition, EAGE, Extended Abstracts, doi: 10.3997/2214-4609.201701689.

Grechka, V., 2007, Multiple cracks in VTI rocks: Effective properties and fracture characterization: Geophysics, **72**, no. 5, D81–D91, doi: 10.1190/1.2751500.

Grechka, V., P. Singh, and I. Das, 2011, Estimation of effective anisotropy simultaneously with locations of microseismic events: Geophysics, **76**, no. 6, WC143–WC155, doi: 10.1190/geo2010-0409.1.

Grechka, V., and S. Yaskevich, 2014, Azimuthal anisotropy in microseismic monitoring: A Bakken case study: Geophysics, **79**, no. 1, KS1–KS12, doi: 10.1190/geo2013-0211.1.

Gupta, I. N., 1973, Dilatancy and premonitory variations of P, S travel times: Bulletin of the Seismological Society of America, **63**, 1157–1161.

Hall, S. A., J.-M. Kendall, J. Maddock, and Q. Fisher, 2008, Crack density tensor inversion for analysis of changes in rock frame architecture: Geophysical Journal International, **173**, 577–592, doi: 10.1111/j.1365-246X.2008.03748.x.

Horne, S. A., 2003, Fracture characterization from walkaround VSPs: Geophysical Prospecting, **51**, 493–499, doi: 10.1046/j.1365-2478.2003.00391.x.

Hudson, J., 1981, Wave speeds and attenuation of elastic waves in material containing cracks: Geophysical Journal of the Royal Astronomical Society, **64**, 133–150, doi: 10.1111/j.1365-246X.1981.tb02662.x.

Jarosiński, M., 2005, Ongoing tectonic reactivation of the Outer Carpathians and its impact on the foreland: Results of borehole breakout measurements in Poland: Tectonophysics, **410**, 189–216, doi: 10.1016/j.tecto.2004.12.040.

Johnston, J. E., and N. I. Christensen, 1995, Seismic anisotropy of shales: Journal of Geophysical Research: Solid Earth, **100**, 5991–6003, doi: 10.1029/95JB00031.

Kendall, J.-M., Q. J. Fisher, S. Covey Crump, J. Maddock, A. Carter, S. A. Hall, J. Wookey, S. L. A. Valcke, M. Casey, G. Lloyd, and W. Ben Ismail, 2007, Seismic anisotropy as an indicator of reservoir quality in siliciclastic rocks: Geological Society of London, Special Publications 292, 123–136.

Kowalski, H., P. Godlewski, W. Kobusinski, W. Makarewicz, M. Podolak, A. Nowicka, Z. Mikolajewski, D. Chase, R. Dafni, A. Canning, and Z. Koren, 2014, Imaging and characterization of a shale reservoir onshore Poland, using full-azimuth seismic depth imaging: First Break, **32**, 101–109.

Liu, E., and A. Martinez, 2012, Seismic fracture characterization: Concepts and practical applications: EAGE.

Lonardelli, I., H.-R. Wenk, and Y. Ren, 2007, Preferred orientation and elastic anisotropy in shales: Geophysics, **72**, no. 2, D33–D40, doi: 10.1190/1.2435966.

Lynn, H. B., W. E. Beckham, K. M. Simon, C. R. Bates, M. Layman, and M. Jones, 1999, P-wave and S-wave azimuthal anisotropy at a naturally fractured gas reservoir, Bluebell-Altamont Field, Utah: Geophysics, **64**, 1312–1328, doi: 10.1190/1.1444636.

Lynn, H. B., and L. Thomsen, 1986, Shear-wave exploration along the principal axis: 56th Annual International Meeting, SEG, Expanded Abstracts, 473–476.

MacBeth, C., 2002, Multi-component VSP analysis for applied seismic anisotropy: Pergamon.

Martin, M. A., and T. L. Davis, 1987, Shear-wave birefringence: A new tool for evaluating fractured reservoirs: The Leading Edge, **6**, 22–28, doi: 10.1190/1.1439333.

Miyazawa, M., R. Snieder, and A. Venkataraman, 2008, Application of seismic interferometry to extract P- and S-wave propagation and observation of shear-wave splitting from noise data at Cold Lake, Alberta, Canada: Geophysics, **73**, no. 4, D35–D40, doi: 10.1190/1.2937172.

Mueller, M. C., 1991, Prediction of lateral variability in fracture intensity using multicomponent shear-wave surface seismic as a precursor to horizontal drilling in the Austin Chalk: Geophysical Journal International, **107**, 409–415, doi: 10.1111/j.1365-246X.1991.tb01402.x.

Mueller, M. C., A. J. Boyd, and C. Esmersoy, 1994, Case studies of the dipole shear anisotropy log: 64th Annual International Meeting, SEG, Expanded Abstracts, 1143–1146.

Naar, W. N., J. B. Schechter, and L. Thompson, 2006, Naturally fractured reservoir characterization: SPE.

Nur, A., and G. Simmons, 1969, Stress-induced velocity anisotropy in rock: An experimental study: Journal of Geophysical Research, **74**, 6667–6674, doi: 10.1029/JB074i027p06667.

Patterson, D., and X. M. Tang, 2001, Shear wave anisotropy measurement using cross-dipole acoustic logging: An overview: Petrophysics, **42**, 107–117.

Rial, J. A., M. Elkibbi, and M. Yang, 2005, Shear-wave splitting as a tool for the characterization of geothermal fractured reservoirs: Lessons learned: Geothermics, **34**, 365–385, doi: 10.1016/j.geothermics.2005.03.001.

Savage, M. K., 1999, Seismic anisotropy and mantle deformation: What have we learned from shear wave splitting? Reviews of Geophysics, **37**, 65–106, doi: 10.1029/98RG02075.

Silver, P. G., and W. W. Chan, 1991, Shear wave splitting and subcontinental mantle deformation: Journal of Geophysical Research: Solid Earth, **96**, 16429–16454, doi: 10.1029/91JB00899.

Tarantola, A., 2005, Inverse problem theory and methods for model parameter estimation: SIAM.

Teanby, N. A., J.-M. Kendall, and M. van der Baan, 2004, Automation of shear-wave splitting measurements using cluster analysis: Bulletin of the Seismological Society of America, **94**, 453–463, doi: 10.1785/0120030123.

Thomsen, L., 1986, Weak elastic anisotropy: Geophysics, **51**, 1954–1966, doi: 10.1190/1.1442051.

Thomsen, L., 2002, Understanding seismic anisotropy in exploration and exploitation: SEG.

Tillotson, P., J. Sothcott, A. I. Best, M. Chapman, and X. Y. Li, 2012, Experimental verification of the fracture density and shear-wave splitting relationship using synthetic silica cemented sandstones with a controlled fracture geometry: Geophysical Prospecting, **60**, 516–525, doi: 10.1111/j.1365-2478.2011.01021.x.

Tsvankin, I., 1997, Anisotropic parameters and P-wave velocity for orthorhombic media: Geophysics, **62**, 1292–1309, doi: 10.1190/1.1444231.

Usher, P. J., A. F. Baird, and J.-M. Kendall, 2015, Shear-wave splitting in highly anisotropic shale gas formations: 85th Annual International Meeting, SEG, Expanded Abstracts, 2435–2439.

Verdon, J. P., D. A. Angus, J.-M. Kendall, and S. A. Hall, 2008, The effect of microstructure and nonlinear stress on anisotropic seismic velocities: Geophysics, **73**, no. 4, D41–D51, doi: 10.1190/1.2931680.

Verdon, J. P., and J.-M. Kendall, 2011, Detection of multiple fracture sets using observations of shear-wave splitting in microseismic data: Geophysical Prospecting, **59**, 593–608, doi: 10.1111/j.1365-2478.2010.00943.x.

Verdon, J. P., J.-M. Kendall, D. J. White, and D. A. Angus, 2011, Linking microseismic event observations with geomechanical models to minimize the risks of storing CO_2 in geological formations: Earth and Planetary Science Letters, **305**, 143–152, doi: 10.1016/j.epsl.2011.02.048.

Verdon, J. P., J.-M. Kendall, and A. Wuestefeld, 2009, Imaging fractures and sedimentary fabrics using shear wave splitting measurements made on passive seismic data: Geophysical Journal International, **179**, 1245–1254, doi: 10.1111/j.1365-246X.2009.04347.x.

Verdon, J. P., and A. Wuestefeld, 2013, Measurement of the normal/tangential fracture compliance ratio (Z_N/Z_T) during hydraulic fracture stimulation using S-wave splitting data: Geophysical Prospecting, **61**, 461–475, doi: 10.1111/j.1365-2478.2012.01132.x.

Vinnik, L. P., R. Kind, G. L. Kosarev, and L. I. Makeyeva, 1989, Azimuthal anisotropy in the lithosphere from observations of long-period S-waves: Geophysical Journal International, **99**, 549–559, doi: 10.1111/j.1365-246X.1989.tb02039.x.

Wang, Z., 2001, Seismic anisotropy in sedimentary rocks: 71st Annual International Meeting, SEG, Expanded Abstracts, 1740–1743.

Willis, H., G. Rethford, and E. Bielanski, 1986, Azimuthal anisotropy: The occurrence and effect on shear wave data quality: 56th Annual International Meeting, SEG, Expanded Abstracts, 479–481.

Wolfe, C. J., and P. G. Silver, 1998, Seismic anisotropy of oceanic upper mantle: Shear wave splitting methodologies and observations: Journal of Geophysical Research: Solid Earth, **103**, 749–771, doi: 10.1029/97JB02023.

Wuestefeld, A., O. Al-Harrasi, J. P. Verdon, J. Wookey, and J. M. Kendall, 2010, A strategy for automated analysis of passive microseismic data to image seismic anisotropy and fracture characteristics: Geophysical Prospecting, **58**, 755–773, doi: 10.1111/j.1365-2478.2010.00891.x.

Wuestefeld, A., J. M. Kendall, J. P. Verdon, and A. van As, 2011, In situ monitoring of rock fracturing using shear wave splitting analysis: An example from a mining setting: Geophysical Journal International, **187**, 848–860, doi: 10.1111/j.1365-246X.2011.05171.x.

Xu, S., and M. S. King, 1989, Shear-wave birefringence and directional permeability in fractured rock: Scientific Drilling, **1**, 27–33.

Wojciech Gajek is a Ph.D. candidate at the Institute of Geophysics Polish Academy of Sciences in Warsaw, Poland. He is working on induced seismicity, and his main research interests include anisotropy estimation, SWS, and velocity model building. Within the secondary branch of his activity, he leads a project on seismic monitoring of calving glaciers.

Michal Malinowski received an M.S. Eng. in exploration geophysics from the AGH University of Science and Technology in Cracow (2000). Since 2001, he has been employed at the Institute of Geophysics Polish Academy of Sciences (IG PAS) in Warsaw, where he also received his Ph.D. (2006). Between 2007 and 2008, he was a visiting fellow at the Geological Survey of Canada in Ottawa. Since 2013, he has been working as an associate professor at IG PAS, and since 2017 he has been head of the Geophysical Imaging Department. He was awarded with the M. P. Rudzki award of the Earth Sciences section of the Polish Academy of Sciences in 2017. His research interests include deep crustal structure, seismic data processing, and imaging, including advanced technologies such as full-waveform inversion.

James P. Verdon received an M.Sci. in natural sciences from Cambridge University and a Ph.D. (2010) in geophysics from the University of Bristol. He is a lecturer in applied geophysics in the School of Earth Sciences, University of Bristol. His research interests include the behavior of fractured rocks as they are affected by underground human activities. This includes the use of geophysical methods to image fractured rocks and, in particular, the use of microseismic monitoring to image geomechanical deformation and the use of statistical and numerical modeling methods to simulate the impacts of human activities in the subsurface.